Automation in Construction 91 (2018) 120–132

Contents lists available at ScienceDirect

Automation in Construction

journal homepage: www.elsevier.com/locate/autcon

Image analysis method for crack distribution and width estimation for reinforced concrete structures

Yuan-Sen Yang[a,b,*], Chiun-lin Wu[b], Thomas T.C. Hsu[c], Hsuan-Chih Yang[b], Hu-Jhong Lu[b], Chang-Ching Chang[b]

[a] Department of Civil Engineering, National Taipei University of Technology, 1 Sec 3 Zhongxiao E Rd, Taipei, Taiwan
[b] National Center for Research on Earthquake Engineering, 200 Sect 3 Xinhai Rd 106, Taipei, Taiwan
[c] Department of Civil and Environmental Engineering, University of Houston, N114 Engineering Building 1, Houston, TX 77204-4003, USA

ARTICLE INFO

Keywords:
Image analysis
Shear crack
Thin crack observation
RC structure
Structural-health monitoring

ABSTRACT

Crack observation is important for evaluating the structural performance and safety of reinforced concrete (RC) structures. Most of the existing image-based crack detection methods are based on edge detection algorithms, which detect cracks that are wide enough to present dark areas in the obtained images. Cracks initiate as thin cracks, generally having width less than the width of a pixel in images; such cracks are generally undetectable by edge detection-based methods.

An image analysis method is proposed to observe the development and distribution of thin cracks on RC surfaces; it also allows estimation of crack widths. Image matching based on optical flow and subpixel is employed to analyze slight concrete surface displacements. Camera calibration is included to eliminate perspective effects and lens distortion. Geometric transformation is adopted so that cameras do not need to be perpendicular to the observed surface or specified positions. Formulas are proposed to estimate the width of shear crack opening. The proposed method was then applied to a cyclic test of an RC structure. The crack widths and their development analyzed by the image analysis were verified with human inspection in the test. In addition, concrete surface cracks that appeared at a very early stage of the test could be observed by the proposed method before they could be detected by the naked eye. The results thus demonstrate that the proposed image analysis method offers an efficient way applicable not only for structural tests but also for crack-based structural-health-monitoring applications.

1. Introduction

Crack observation is an important aspect of most reinforced concrete (RC) structural experiments and structural safety evaluation. The crack patterns, angles, and distribution density may reveal the failure modes, damage levels, and stiffness degradation for concrete models [1,2]. The effect of cracks on structural strength or water permeability has been discussed in many studies [3,4]. The reasonable limits of crack widths and repair methods have been recommended by standard codes or regulations [5,6]. In addition, for the containment vessel of a nuclear reactor, cracks indicate the risk of radiation leak [7]; therefore, regulations have been established [8]. While many numerical models of concrete materials adopt the concept of smeared cracks to estimate crack-induced strength degradation (e.g., [9]), some methods involve simulation of concrete cracks and numerical analysis of crack widths for better prediction of crack-induced structural behaviors [10,11].

Since the advancement of digital image technology, image analysis methods have been utilized for crack detection as they provide more advantages and feasibility for structural health monitoring (SHM) applications. Image analysis offers a cost-effective, alternative solution to concrete crack observation and has potential in SHM applications. Using image analysis, we can not only record the overall visual appearance of an RC surface but also analyze vibrations [12], deformation [13,14], and terrain models [15] as well as assess construction quality such as welding quality [16] or loosened bolts [17]. Structural deformations, mode shapes, natural frequencies, and motion magnification can also be estimated using image analysis [18]. Image analysis has been also employed to detect cracks. Yu et al. [19] analyzed infrared images to detect tunnel lining surface cracks. Hutchinson and Chen [20] conducted image analysis to evaluate concrete damage of bridges induced by cracks and spalling. Zakeri et al. [21] developed an approach to interpret and classify pavement cracks. Chen et al. [22] recognized cracks through analyzing hundreds of photos in a bridge management database. Li et al. [23] recognized bridge cracks through

* Corresponding author at: Department of Civil Engineering, National Taipei University of Technology, 1 Sec 3 Zhongxiao E Rd, Taipei, Taiwan.
E-mail address: ysyang@ntut.edu.tw (Y.-S. Yang).

https://doi.org/10.1016/j.autcon.2018.03.012
Received 10 May 2017; Received in revised form 22 January 2018; Accepted 4 March 2018

image edge detection and noise reduction. Dinh et al. [24] proposed a method to extract concrete cracks based on the image gray-scale histogram. Machine-learning-based computer vision has been applied and trained to detect concrete cracks under various environmental conditions, e.g., Prasanna et al. [25] and Cha et al. [26]; it is capable of detecting a wide variety of concrete surface defects as well as reducing the effects of uncontrollable ambient lights, provided that sufficient training data are available. Most of the existing crack detection methods are based on edge detection, which extracts the dark shadow lines or crack regions.

However, these methods are suitable for observing only wide cracks that present dark lines in the images, but not for thin cracks that do not present dark lines in the images or in cases where the camera is located too far from a specimen for the dark lines to appear.

Crack width is not easy to measure on the basis of the number of dark pixels or the pixel intensity if the crack is thinner than about one pixel in an image. Cracks appear dark because they do not reflect light. In an image, the boundary of a crack is at a gray level between dark (corresponding to the crack) and light (corresponding to the intact concrete surface), indicating that only a part of the gray pixel corresponds to the crack. If a crack is thinner than one pixel, it only appears as a gray line in an image. The pixel intensity does not represent the area occupied by the crack because it depends on not only the crack width but also the light in the environment, exposure time and aperture of the camera, and many other factors.

A preliminary test [27] showed that cracks that are thinner than about one-third of a pixel in an image cannot be recognized. This preliminary image test (Fig. 1) showed that a 0.15 mm dark line printed on a crack width ruler cannot be recognized clearly even in images captured using a high-resolution digital camera (e.g., 22 MP) at a close object distance (< 2 m). The equivalent pixel size is about 0.45 mm per pixel, i.e., the crack width corresponding to a 0.33-pixel crack is about 0.15 mm. In this paper, a thin crack is defined as a crack whose width is as small as 0.1 mm and is invisible in photos taken in this study. In possible future SHM applications, 0.1-mm cracks are still invisible in photos, even if a 100-mega-pixel camera is used to monitor a 6-meter-wide area.

In addition to being used in structural safety evaluation, image analysis of crack development can be applied in structural laboratories. In a concrete structure test, the development of surface cracks is typically observed and recorded by pausing the test and the inspectors manually sketching lines on the crack surfaces, which is time consuming, labor intensive, and risky at a certain level. While the hydraulic actuators that apply force on the specimen appear fixed and stable, they in fact move back-and-forth within a small displacement range and are controlled hydraulically at a high frequency, rather than being physically fixed. A long experiment pause could result in stress relaxation in the specimen, leading to inconsistent or inaccurate experimental results [28].

This study proposes an image analysis method that can estimate shear crack opening fields on an RC surface. This method is based on the surface displacement field measurement that was previously developed and has been applied to many experiments [29]. Surface displacement field measurements are applied to observe horizontal flexural cracks. In this paper, we present the geometric transformation between the observed surface and the cameras and the analysis of the crack widths according to the displacements measured using image analysis. In addition, we compare manual estimation and image analysis of cracks.

2. Analysis procedures and formulas

The image analysis method that was employed and modified in this work has been implemented in a program named ImPro Stereo [30,31]. This method generally consists of four major steps: stereo calibration of two cameras, three-dimensional (3D) control point positioning, metric image rectification, and surface displacement and deformation analysis. Stereo calibration is carried out to estimate the intrinsic and extrinsic parameters of cameras, including coordinate system transformation relationships between cameras, focal lens, and distortion coefficients. Thus, the calibration provides sufficient parameters to carry out coordinate transformation between image coordinates and a 3D coordinate system. Stereo calibration is performed using a self-calibration method implemented by Bouguet [32] and OpenCV [33,34], which only requires a planar board such as a chessboard rather than a 3D calibration apparatus. Therefore, the ease of calibration is increased, thereby improving the wide applications of image analysis in engineering. Note that since the parameters obtained by the stereo calibration are critically important in the follow-up calculation, this method requires the focal lengths and positions of both cameras to be fixed during the measurement.

3D control point positioning is used to determine four control points of a part of a cylindrical surface (named the region of interest, ROI) by using image tracking with sub-pixel accuracy and stereo triangulation techniques, as shown in Fig. 2(a). A cylindrical coordinate is then defined by determining the cylindrical surface parameters, including the central axis, the reference origin, and the radius of the cylinder, as shown in Fig. 2(b). Then, the ROI can be mathematically described on the basis of the cylindrical coordinate. The mathematical procedure for determining the parameters of a cylindrical surface is outlined in

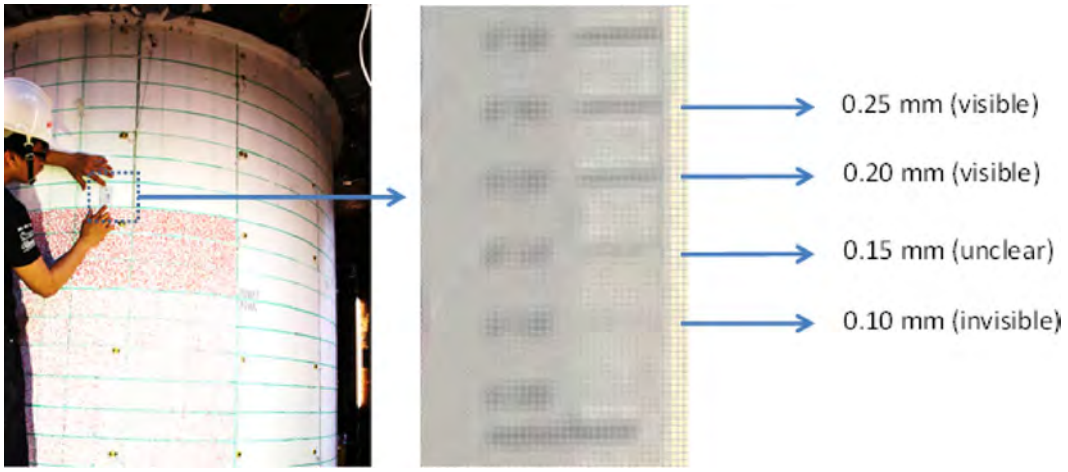

(a) A photo of the crack ruler image test (b) Zoomed image of crack width ruler lines

Fig. 1. Minimally recognizable cracks in images taken in the test [27].

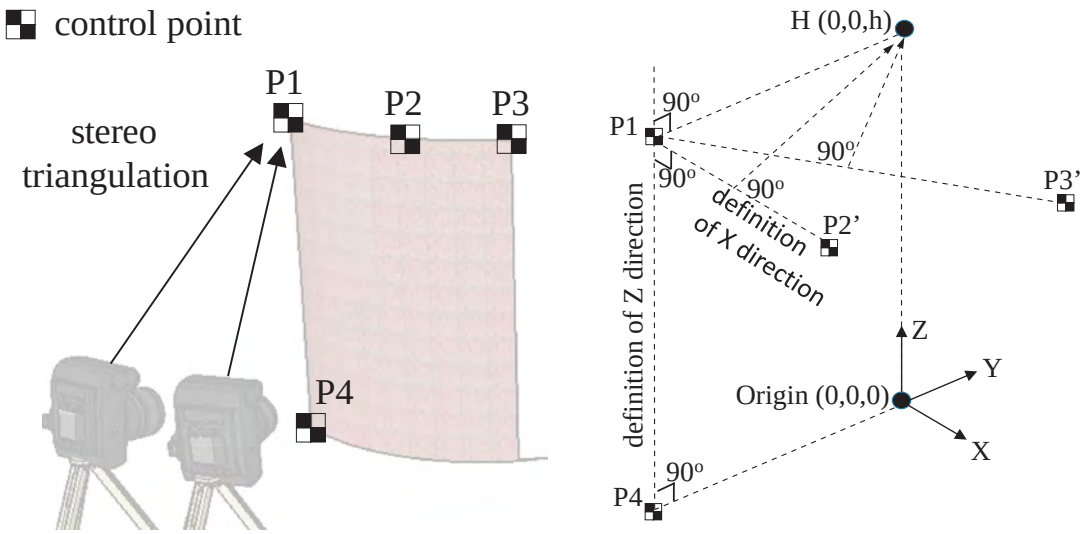

(a) Four control points on a cylindrical surface (b) A cylindrical coordinate

Fig. 2. Control point positioning using stereo triangulation.

Table 1
Algorithm to determine cylindrical surface parameters.

INPUT: Four control points *P1*, *P2*, *P3*, and *P4*, where each point is represented by a 3-by-1 vector.
OUTPUT: Cylindrical surface parameters *Origin*, *h*, *r*, v_x, v_y, v_z, and θ.
Step 1 Set v_z = normalize ($P1 - P4$) and h = norm ($P1 - P4$)
Step 2 Set v_{x12} = normalize ($P2 - P1$)
Step 3 Set v_{y12} = normalize (cross (v_z, v_{x12}))
Step 4 Set v_{x12P} = normalize (cross (v_{y12}, v_z))
Step 5 Set v_{x13} = normalize ($P3 - P1$)
Step 6 Set v_{y13} = normalize (cross (v_z, v_{x13}))
Step 7 Set v_{x13P} = normalize (cross (v_{y13}, v_z))
Step 8 Set $P_{2P} = P1$ + dot ($P2 - P1$, v_{x12P}) v_{x12P}
Step 9 Set $P_{3P} = P1$ + dot ($P3 - P1$, v_{x13P}) v_{x13P}
Step 10 Set $P_{12PMid} = 0.5\ (P1 + P_{2P})$
Step 11 Set $P_{13PMid} = 0.5\ (P1 + P_{3P})$
Step 12 Set a 3-by-1 vector $B = P_{12PMid} - P_{13PMid}$
Step 13 Set a 3-by-2 matrix $A = [v_{y12} - v_{y13}]$
Step 14 Solve $F = (A^TA)^{-1}\ (A^TB)$
Step 15 Set f_1 and f_2 as the first and second elements of vector F, respectively.
Step 16 Set $H = 0.5\ (P_{12PMid} + f_1\ v_{y12}) + 0.5\ (P_{13PMid} + f_2\ v_{y13})$
Step 17 Set v_x = normalize ($P1 - H$)
Step 18 Set r = norm ($P1 - H$)
Step 19 Set v_y = normalize (cross (v_z, v_x))
Step 20 Set $\theta = \cos^{-1}$ (dot (v_x, normalize ($P_{3P} - H$)))
Step 21 Set *Origin* = H – norm ($P1 - P4$) v_z

Table 1.

Metric rectification is then applied to convert the image of the ROI surface to a plane image through a series of resampling processes. Metric rectification is required for mapping a curved ROI surface to a plane image so that follow-up image analysis procedures can be processed. Each resampling process generates a pixel, and the entire rectified image normally requires millions of resampling processes.

Finally, optical flow analysis is employed to analyze the displacement field of the images by comparing the rectified image at the current state with that at the initial state. Optical flow analysis tracks movements of objects in a video or a time series of images, and it can be applied for traffic analysis [35], detection of concrete tube defects [36], etc. Cha et al. [37] adopted optical flow and unscented Kalman filter to reduce the measured displacement noise. In addition to the optical flow analysis, digital image correlation methods and feature-based methods are used for displacement of the control points. Digital image correlation splits the image of an un-deformed object into a grid of sub-images and determines the displacements and deformation parameters by iteratively searching similar sub-images in the image of the deformed object [38]. However, the computation of the digital image correlation method is extremely time consuming for image searching; therefore, we did not use it in this work. Feature-based methods generally comprise feature detection, extraction, and matching techniques; they have been used to estimate the deformation of objects in medical images, 3D building scene registration [39], and many other applications. Feature-based methods were not employed in this work because they only match detected feature points and do not process the arbitrary points that we require.

This study developed a procedure to estimate the crack opening field according to the displacement field analyzed by the aforementioned metric rectification and optical flow analysis processes. As mentioned, a crack opening can be associated with the related displacement in a rotated coordinate system. The analyzed displacement field is a discretized mesh, representing the displacement field of an ROI. Each cell contains two numbers, U_x and U_y, representing the horizontal and vertical displacements of a discrete cell, respectively. Fig. 3 shows the crack opening model used in this study. A crack may induce a crack opening c_o and a crack sliding c_s. The crack separates a surface into two parts, say, part A and part B. Assuming that the crack is ideally represented by two parallel lines in a small region (approximately near the cell marked O in Fig. 3), the crack opening width is the gap between these two lines; meanwhile, the crack sliding is the related movement parallel to the crack between the two parts.

Assuming that the displacement fields around cell O are mainly induced by the crack, we ignore the relatively small deformation of

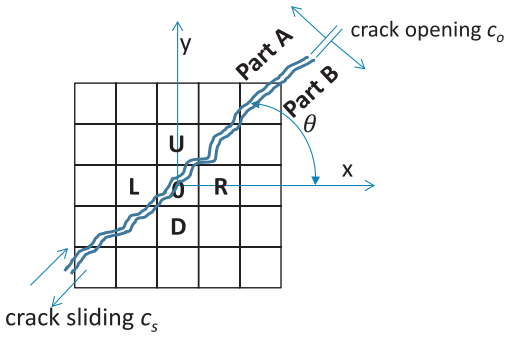

Fig. 3. The crack opening model used in this study.

parts A and B. In Fig. 3, U, D, L, and R refer to the up, down, left, and right cells relative to cell O, respectively. The displacements of parts A and B can be estimated by a weighted average of cells U and L and R and D, respectively. The following equations are estimated for $0^\circ \le \theta < 90^\circ$:

$$U_A \cong \frac{U_U \cos\theta + U_L \sin\theta}{\cos\theta + \sin\theta} \quad (1)$$

$$U_B \cong \frac{U_D \cos\theta + U_R \sin\theta}{\cos\theta + \sin\theta} \quad (2)$$

For $90^\circ \le \theta < 180^\circ$, the equations become

$$U_A \cong \frac{-U_D \cos\theta + U_L \sin\theta}{\cos\theta + \sin\theta} \quad (3)$$

$$U_B \cong \frac{-U_U \cos\theta + U_R \sin\theta}{\cos\theta + \sin\theta} \quad (4)$$

The relationship between the crack opening, sliding, and displacements of parts A and B can be expressed by Eq. (5), where the subscripts x and y denote the x and y components, respectively.

$$\begin{bmatrix} \cos(\theta + \pi/2) & \cos\theta \\ \sin(\theta + \pi/2) & \sin\theta \end{bmatrix} \begin{bmatrix} c_o \\ c_s \end{bmatrix} = \begin{bmatrix} U_{Ax} - U_{Bx} \\ U_{Ay} - U_{By} \end{bmatrix} \quad (5)$$

The crack opening c_o of cell O shown in Fig. 4 can be obtained by solving the 2-by-2 linear equations. The crack opening field of the entire ROI can be estimated by calculating the crack openings of all the cells in the mesh.

The image analysis procedure has been implemented into the software named ImPro Stereo (Fig. 4), developed in the MATLAB environment. The camera calibration and stereo triangulation implemented in ImPro Stereo are based on Bouguet's toolbox [32]. The optical flow analysis and many other image manipulations (e.g., image resizing, remapping, and template matching) are based on OpenCV through the MATLAB executable technique.

3. Experimental setup

In the structural experiment conducted in this study, a reduced-scale RC containment vessel was subjected to a cyclic loading at the top. The height, outer diameter, and thickness of the cylindrical tube RC structure were 2.25 m, 2.5 m, and 0.15 m, respectively. The tube was fixed with rigid RC blocks at its top and bottom. Fig. 5 shows the basic dimensions of the specimen. A vertical downward load was applied by four vertical actuators to simulate the gravity load on the tube imparted by the upper structure. The displacement of top RC block was simply controlled using eight hydraulic actuators with a cyclic displacement history along a horizontal degree of freedom (say X) and controlled with zero rotations and torsion. Fig. 6(a) presents the schematic representation of the specimen clamped by actuators, the steel clampers (red), and the location of the cameras. Fig. 6(b) shows an actual photo of the specimen, protection frame, clampers, actuators, data loggers, controllers, and cameras. Unrelated background has been cropped from the photo. The measurement equipment and sensors include 176 strain gauges attached on the reinforcing bars, 120 3D optical tracking points, and two sets of stereo imaging systems. This study focuses on the stereo imaging system that is located at the north side of the specimen.

Two Canon EOS 5D Mark III digital cameras featuring a 22-megapixel sensor were setup as a stereo imaging system on the north lateral side of the specimen; these cameras measured the deformation and observed the crack distributions of the ROI during the experiment. Fig. 6(a) shows the location of the ROI relative to the specimen.

The ROI occupied one eighth of the perimeter and about half of the height (Fig. 7(a)). It was approximately 0.97 m wide and 1.4 m high (Fig. 7(b)). A randomly featured pattern was painted in red on the ROI for image analysis (see Fig. 7(c)) so that each cell in the rectified images has its unique image pattern and can be correctly identified in the image analysis. Four control point marks (Fig. 7(d)) were attached along the boundary of the ROI. These control points were then positioned by stereo triangulation. Their coordinates were required for metric rectification.

This method requires random paintings, stains, spalls, or image features distributed over the measured surface. For future SHM applications, in the set-up phase, a pre-painted pattern needs to be applied on the surfaces of walls, beams, columns, joints, or other regions to be monitored. Geometric measurement based on structured light projection is a popular approach for 3D scanning without painting a pattern on the surface and it has been applied to a wide variety of applications, such as entertainment and reverse engineering. Nonis et al. [40] employed a similar process for concrete spalling examination. However, this approach does not measure a minor displacement of a flat surface in the in-plane directions, because in-plane movement does not change the reflection of structured light. Cracks are typically discontinuous in-plane displacements and cannot be detected with a structured-light-projection approach.

The parameters of the cameras were calibrated with a chessboard-like grid, as shown in Fig. 8(a). Each square in the grid was

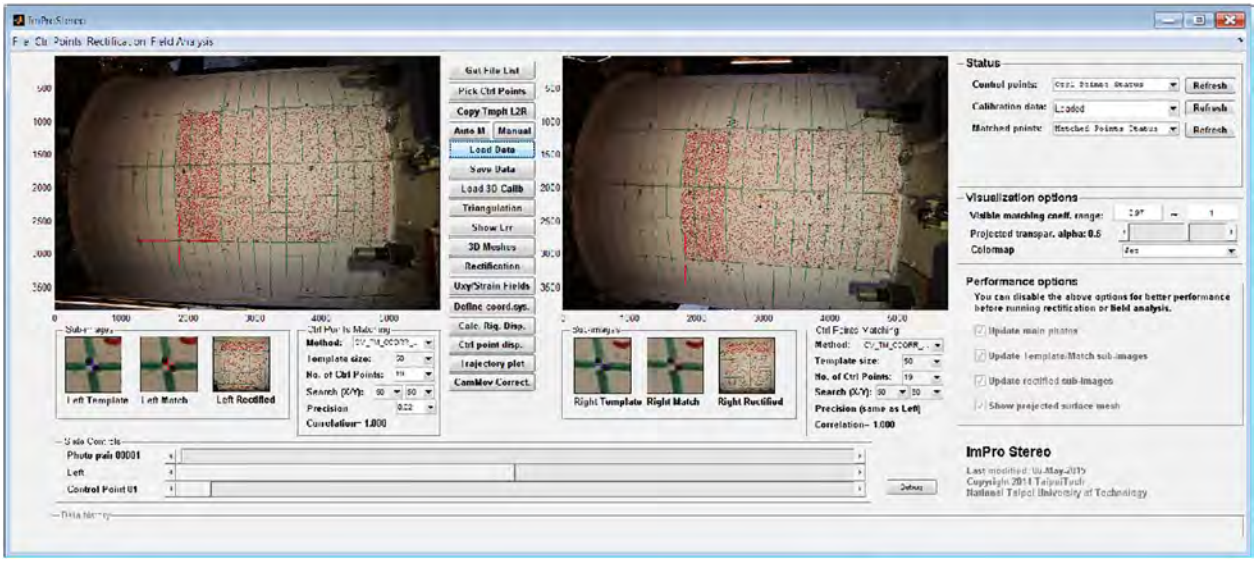

Fig. 4. The user interface of ImPro Stereo.

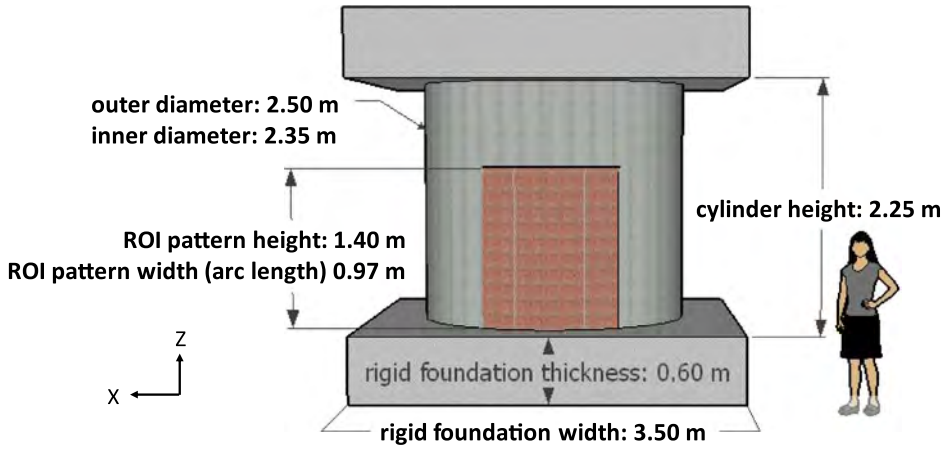

Fig. 5. Specimen and the ROI dimensions.

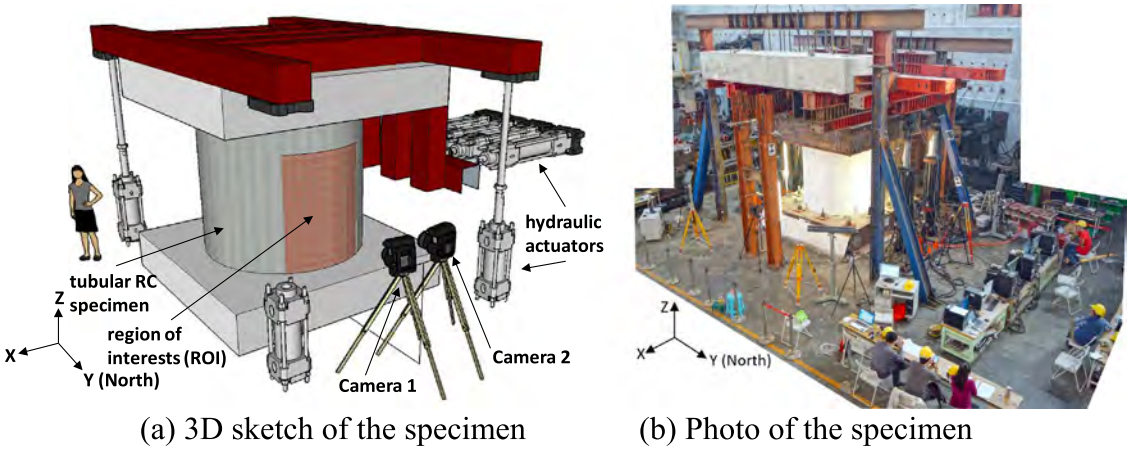

Fig. 6. Specimen and measurement setup. (For interpretation of the references to color in this figure, the reader is referred to the web version of this article.)

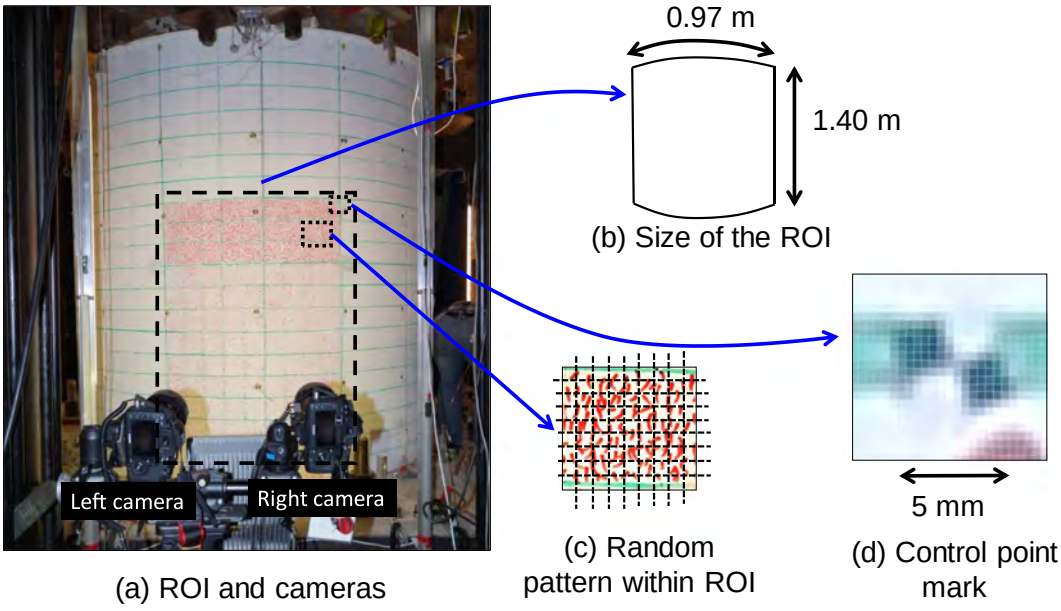

Fig. 7. Surface processing before testing.

99.9 mm × 99.9 mm. The size of the square in the calibration board was the only aspect that was physically measured via the conventional method (using a ruler), while all other data were all measured by image analysis. The calibration was conducted using the Bouguet's camera calibration toolbox [32]. Calibration results include the intrinsic parameters of each camera, such as the focal length, principal point, and

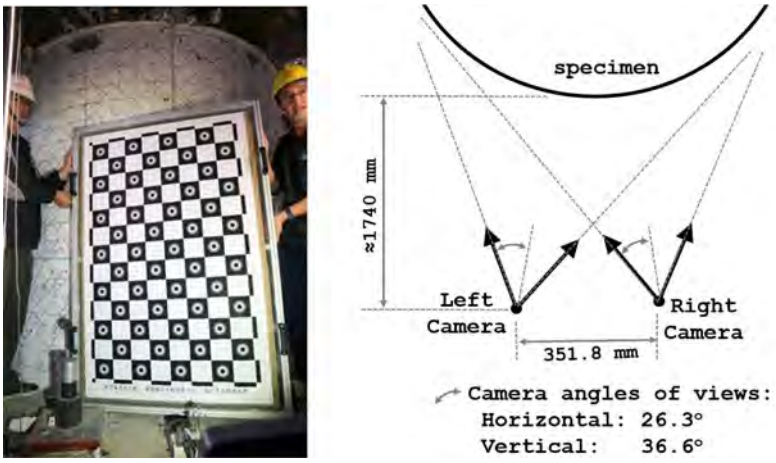

(a) Calibration board (b) Basic calibrated geometric information of cameras

Fig. 8. Camera calibration. (For interpretation of the references to color in this figure, the reader is referred to the web version of this article.)

distortion coefficient, and the extrinsic parameters between the two cameras, which give the coordinate transformation between them. A mathematical model was formed using the intrinsic parameters to describe how objects in the real world would be projected in the image. The extrinsic parameters were required for stereo triangulation and metric rectification. Fig. 8(b) shows some basic geometric information calculated by the calibrated parameters. The distance between the two cameras was 351.8 mm. The angles of view of both cameras were 26.3° horizontally and 36.6° vertically. The distance between the cameras and the specimen was approximately 1740 mm.

4. Experimental results

In the experiment, a cyclic displacement history was applied through 720 hydraulic actuator control steps, as denoted by the blue solid line in Fig. 9. The stereo imaging systems were triggered to capture photos every three to five steps and at each peak of the displacement history (denoted by the green dots in Fig. 9). The reason that the cameras were not triggered every single step was that they need a few seconds to get ready for the next trigger, which was longer than the time of each hydraulic actuator control step. A total of 163 images were captured. The experiment was paused for crack marking at a drift ratio of 0.25%, −0.25%, 0.375%, −0.375%, 0.5%, −0.5%, and 0.75%, as denoted by the red squares in Fig. 9. The crack marking was carried out for regions outside the ROI of image analysis. No further crack marking was done beyond 0.75% drift ratio owing to safety issues, as the applied forces were close to the estimated ultimate strength of the specimen.

Stereo triangulation of control points and metric rectification of the ROI were carried out in the crack analysis. The image positions of the four control points were obtained using a multilevel template matching method [30], which achieves sub-pixel precision (Fig. 10(a) and (b)). The 3D positions were calculated using stereo triangulation. The shape of the cylindrical surface was determined according to the control point positioning (Fig. 10(c)). The metric rectified image was generated by performing image re-sampling of the photos taken by the left camera (e.g., Fig. 10(d)). Each pixel in the rectified image represents a 0.4636 mm × 0.4636 mm area on the ROI surface. The intrinsic and extrinsic parameters that were obtained during camera calibration were used for stereo triangulation and metric rectification.

As mentioned in Eqs. (1)–(5), crack analysis is performed based on displacement fields. The displacement fields of the ROI (Fig. 10(c)) were obtained by comparing the rectified image obtained at a certain step (Fig. 11(b)) with that obtained at the first (initial) step (Fig. 11(a)) by using pyramid optical flow analysis, whose implementation is provided by the OpenCV library. The pyramid optical flow analysis is a well-optimized implementation that can efficiently capture the difference between two images and estimate the movements of multiple points. Fig. 11 shows the progress of this method in processing rectified images generated using the aforementioned procedure. Crack opening fields were obtained (Fig. 11(d)) by analyzing the displacement fields. It is difficult to recognize any cracks clearly on the displacement fields (Fig. 11(c)) without using the calculations given in Eqs. (1)–(5). Fig. 11(d) clearly shows that the crack opening field can be obtained after the crack opening calculation is completed. We can further project

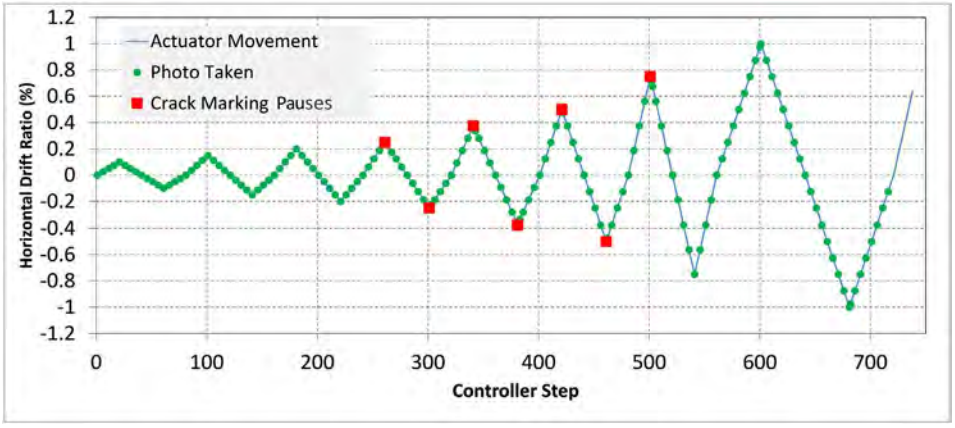

Fig. 9. Cyclic displacement history applied to the top of the specimen. (For interpretation of the references to color in this figure, the reader is referred to the web version of this article.)

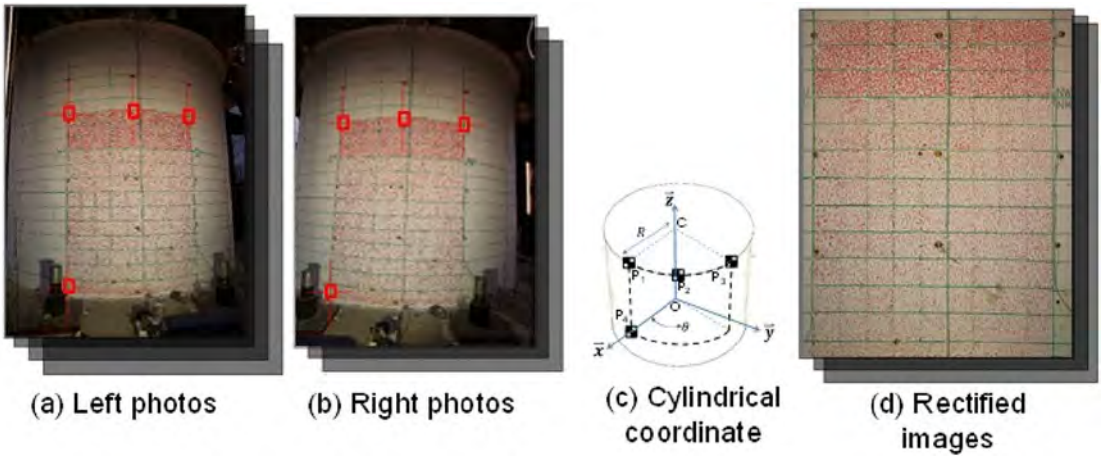

Fig. 10. Control point positioning and metric rectification.

it back to the image for visualization (Fig. 11(e)).

The analysis of crack opening fields by ImPro Stereo based on Eqs. (1)–(5) was carried out through 163 image-capturing steps (excluding the first step, set as the initial condition). Theta was set to either 45° (0.25 π radians) or 135° (0.75 π radians) according to the top displacement. In the crack opening fields, concentration lines of the deformation of the ROI are actually shown. However, the authors believe that for a brittle material such as concrete, the concentration lines of deformation are actually cracks. The crack opening fields provided continuous crack development during the experiment.

In this study, crack opening widths of the ROI were estimated from both manual crack marking and image analysis at seven crack marking pause steps. During manual marking, crack opening widths were estimated using a crack width ruler. Although the cracks in the ROI were also marked manually, they were marked on paper rather than directly on the ROI surface in order to avoid disturbance due to the pen strokes on the image pattern on the ROI. Fig. 12(a) shows the ROI crack markings made at the first suspension (i.e., the red square at step 261 shown in Fig. 9). Compared with the crack opening field (Fig. 12(b)) that was analyzed from images, all 18 manually marked cracks could be found in the image analysis result. The crack opening field revealed more cracks, ranging from 19 to 23, that were not recorded in the manual crack marking. The image-analyzed fields, as shown in Fig. 12(b), were discretized to a mesh having 120 × 80 cells. Since the ROI was about 140 cm × 97 cm, each cell had approximate dimensions of 11.7 mm × 12.1 mm.

Fig. 13 shows the crack distribution of the second suspension (i.e., the second red square in Fig. 9 or step 301). Although the cracks numbered 19–22 in image analysis (Fig. 13(b)) were not recorded during manual crack marking (Fig. 13(a)), this does not imply that they were invisible to the naked eye. According to the image analysis in this case, the crack opening width ranged 0.07–0.1 mm; such cracks may be visible with careful inspection. However, these cracks were not marked likely because they were situated at an inaccessible position for the inspector to locate them. As mentioned above, the space was limited due to experimental clampers and sensor wires.

The opening width of a crack does not remain constant over the entire crack but may vary at different parts of a crack. Each crack in the manual crack marking had a single value of recorded opening width measured by the inspector. However, the width was measured subjectively; that is, the location for measuring the crack opening width was subjectively determined. An inspector was requested to record only a single value of a crack width because of time limitations. For example, crack number 6 shown in Fig. 14, which represents the crack distribution at step 341 (the third red square in Fig. 9), was longer than 1 m. Image analysis (Fig. 14(b)) revealed that the crack opening width varies from 0.08 to 0.18 mm at different locations. Manual markings only recorded it a single crack opening width of 0.15 mm. It should be noted that in the manual crack marking shown in Fig. 14(a), the inspector took about 40 min to examine, mark, and measure a single value of crack opening width for each crack in the ROI. Hence, the time would be impractically longer if the inspector was requested to measure crack opening widths at different locations of a crack. The variations of crack opening widths can only be observed by image analysis results.

Table 2 lists the crack opening records observed manually and by image analysis of the crack distribution at step 381 (the fourth suspension in the test, as indicated by the fourth red square in Fig. 9). The crack distribution result is presented in Fig. 15. The crack opening

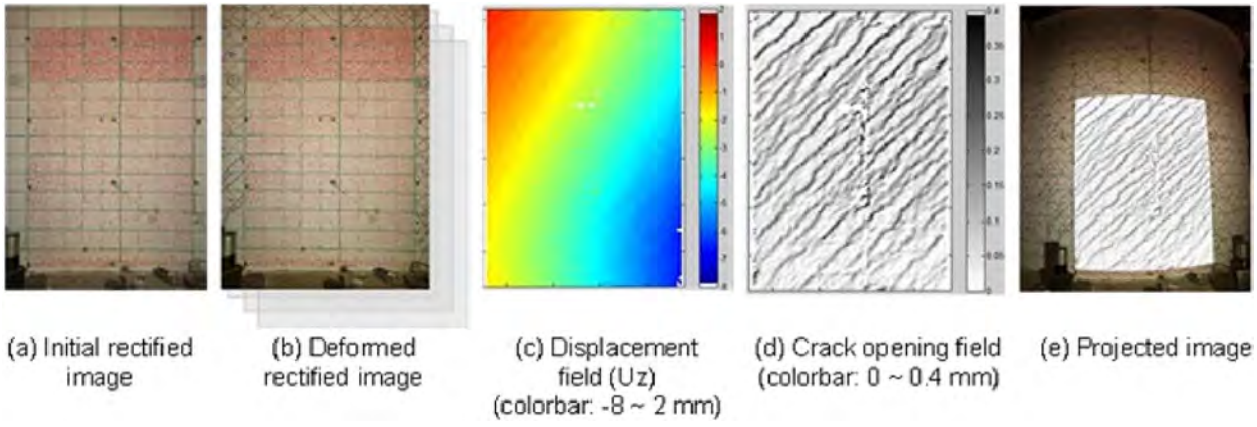

Fig. 11. Crack opening field analysis.

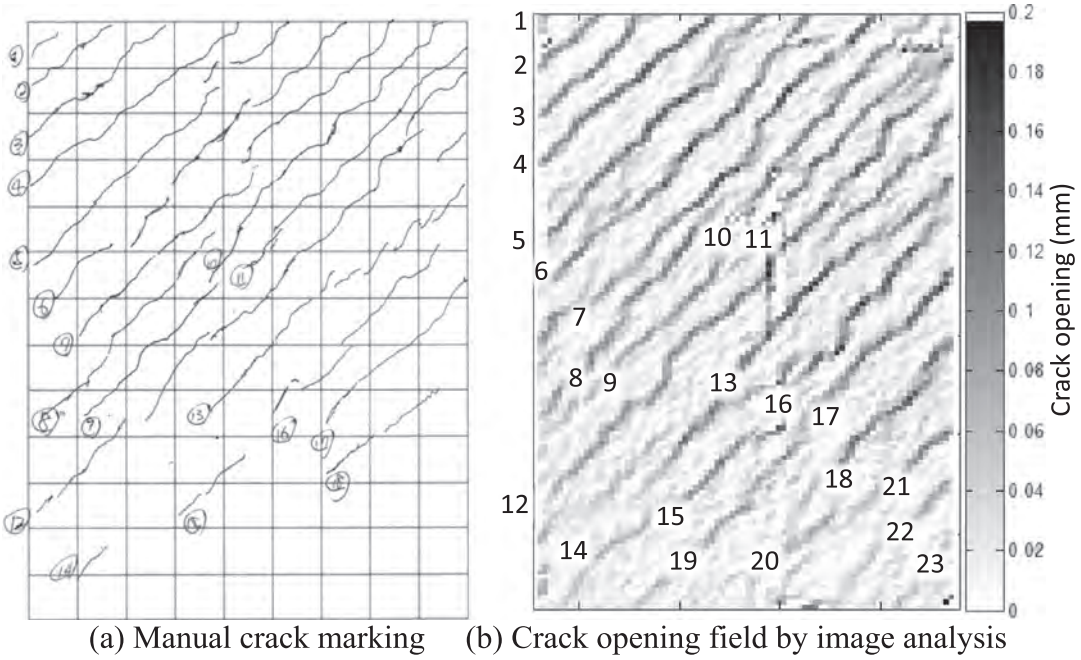

(a) Manual crack marking (b) Crack opening field by image analysis

Fig. 12. Crack distribution: manual crack marking vs. image analysis (drift ratio: +0.25%).

width was measured by the inspector by subjectively determining the measurement location. The crack opening widths obtained by image analysis listed in Table 2 represent the maximal value of a crack opening on a crack. To avoid measurement noise, the maximal value that did not have at least two equal or larger neighboring values was ignored. That is, the image-analyzed values listed in Table 2 have at least two equal or higher neighboring values. Thus, the crack opening widths obtained by image analysis are mostly slightly larger than the manually measured values, possibly because image analysis is less likely to miss the largest crack opening part of a crack.

While the image analysis method is capable of providing more information about crack development and their opening widths, it is sensitive to light noise. All the images analyzed in this study captured a noise signal at some parts of an ROI. Fig. 16(a) shows the crack distribution at step 421 (i.e., the fifth suspension of the test). The red rectangles in Fig. 16(b) indicate the noise obtained by image analysis. This noise was induced by the wires of the conventional sensors. Even a small movement of the wires induced a large amount of noise in the image analysis. The image analysis used in this study is sensitive to slight movement of things, but cannot differentiate between concrete movement and wire movement. Meanwhile, a human inspector is capable of understanding the actual situation, and would not be affected by the wires attached on the surface.

In addition to the seven suspension points, image analysis could analyze the crack development from photos captured at the 163 photographic steps of the entire experiment. The image analysis of a crack

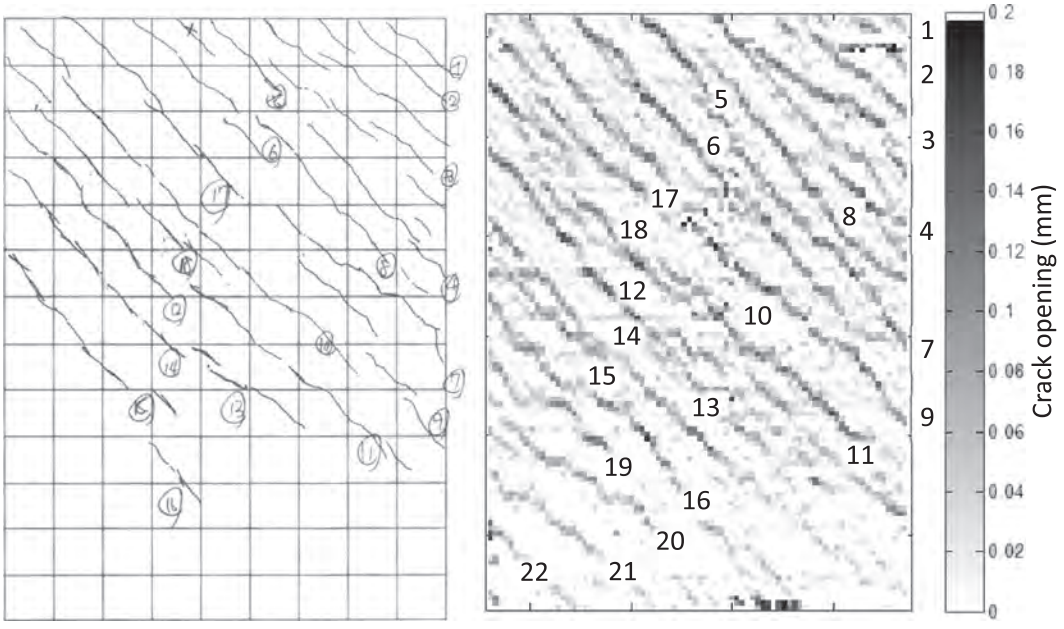

(a) Manual crack marking (b) Crack opening field by image analysis

Fig. 13. Crack distribution: manual crack marking vs. image analysis (drift ratio: −0.25%).

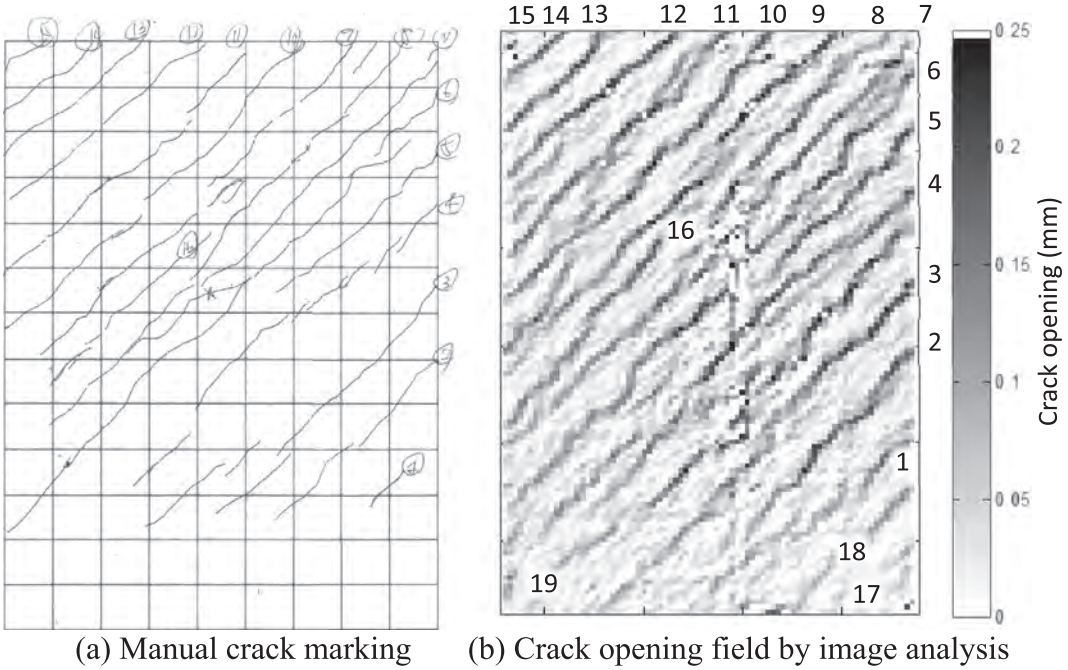

Fig. 14. Crack distribution: manual crack marking vs. image analysis (drift ratio: +0.375%).

Table 2
Crack opening: manual crack marking vs. image analysis (drift ratio: −0.375%).

Crack number	Crack opening by manual measurements (mm)[a]	Crack opening by image analysis (mm)
1	0.1	0.11
2	0.15	0.19
3	0.15	0.18
4	0.15	0.14
5	0.15	0.17
6	0.15	0.19
7	0.15	0.20
8	0.15	0.17
9	0.15	0.20
10	0.15	0.17
11	0.15	0.12
12	0.1	0.12
13	0.15	0.09
14	0.15	0.13
15	0.1	0.16
16	Not recorded	0.10

[a] A crack opening width measured manually must be a multiple of 0.05 because only dark lines of these widths are printed on the crack ruler.

opening field (left plot of Fig. 17) shows that a thin crack with an opening width of only 0.03 mm as well as cracks with an opening width of 0.02 mm could be observed clearly. These cracks were observed when the drift ratio was 0.05%. The middle and right plots in Fig. 17 show the cracks at the beginning phase of the experiment, when no significant cracks were expected at this small drift ratio; these cracks that were as thin as 0.02 mm were invisible to naked eye. Neither the naked eye nor normal digital cameras could directly observe the dark lines of these thin cracks easily.

Fig. 18 shows the observed cracks when the drift ratio reached 0.1%. The thin cracks that were observed in Fig. 18 (at a drift ratio of 0.05%) widened as the drift ratio reached 0.1%. More than ten cracks with openings ranging 0.02–0.05 mm were presented clearly.

If a conventional shear strain measurement method is used, which is also implemented in ImPro Stereo, the cracks can be presented by observing high shear strain lines, but the crack widths cannot be easily converted from the shear strain values. Fig. 19 shows a demonstration of measured shear strain field at drift ratio of 0.1%. Comparing Figs. 18 and 19, crack widths are calculated and seem more apparently to be observed using the proposed method (Fig. 18).

As 163 photographic steps were involved in the experiment, the progress of crack development could be observed and visualized by generating a video showing the 162 steps (excluding the first step that was considered as the initial state). Fig. 20 presents variations of the crack opening widths of five selected cracks (i.e., crack numbers 2–6 in Fig. 12(b)). The cracks opened when the actuator was pushing (i.e., at positive displacement) and closed when the actuator was pulling (i.e., at negative displacement). As these 45° cracks closed, other 135° cracks began to open. The cracks opened and closed in smooth manner until about controller step 550, from where on they became less smooth. This was mainly due to the commencement of severe slipping failure. The continuous crack development video generated in this study is provided at https://youtu.be/8ahXyU5DxOg.

The image analysis was performed offline after the experiment was completed, as a long computing time was required (about 3 h in this case). Although a trained user of ImPro Stereo only took a few minutes for operating this software, the remaining time was taken by the computer for computing the image analysis. Nearly 80% of the computing time was spent on metric rectification, which converts images of cylindrical surfaces in distorted photos to undistorted planes. Each pixel of a rectified image was generated by projecting from a 3D point to a 2D image point, followed by remapping the image point to interpolated color intensities. Table 3 lists the computing time that ImPro Stereo used to run each phase. Manual operation is carried out once and does not scale up with number of photos and their image resolution. Computing time for 163 photographic steps of measurement was approximately 3.5 h, that is, about 95 s per step of measurement (using one set of 22-mega-pixel stereo camera). The computing time roughly grows linearly with the resolution of images and number of cameras to be used. Compared to the total time of 7.1 h that was required by the seven suspensions dedicated for crack marking in the experiment, the image analysis time was relatively small. In addition, because image analysis can be conducted after the experiment, the execution of the experiment would not be affected. Time statistics were measured on a laptop

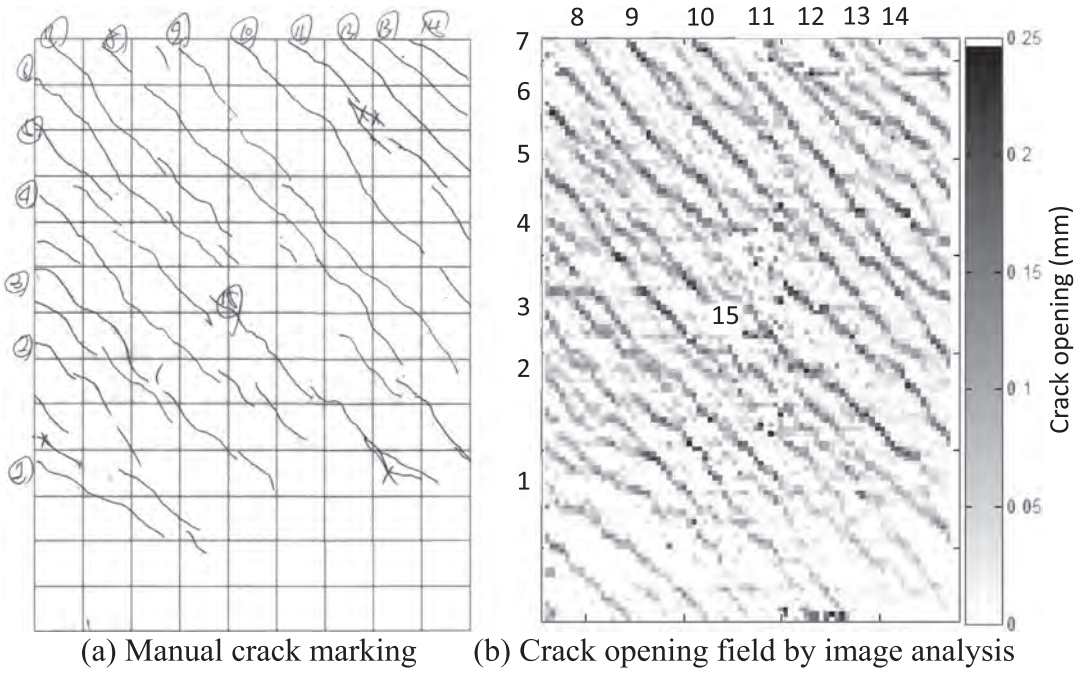

Fig. 15. Crack distribution: manual crack marking vs. image analysis (drift ratio: −0.375%).

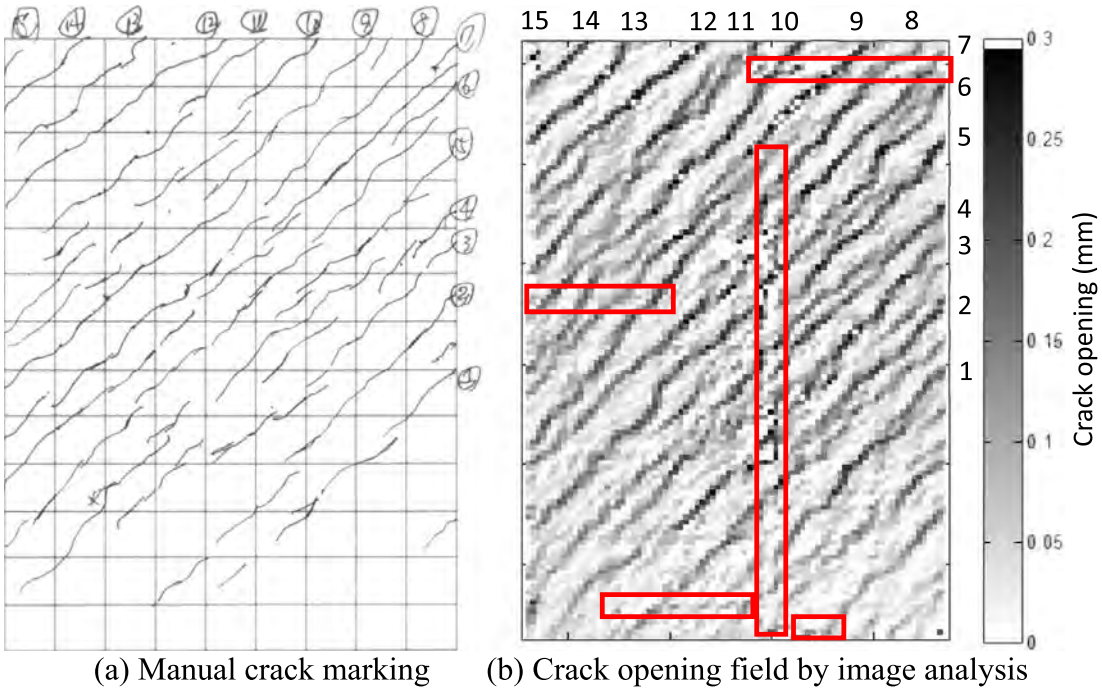

Fig. 16. Crack distribution: manual crack marking vs. image analysis (drift ratio: +0.5%). (For interpretation of the references to color in this figure, the reader is referred to the web version of this article.)

equipped with a 2.4 GHz Intel i7 processor, 16 GB main memory, Windows 7, and MATLAB 2009a. If a larger ROI is chosen, more stereo camera systems with higher resolution cameras could be used and the computing time would grow linearly with the number of pixels to process. For example, measuring a 6-meter-by-4-meter ROI using 8 sets of 50-mega-pixel stereo cameras, the computing time could be about 18 times longer of this experiment, i.e., half an hour of computing time per measurement step. Future efforts would address the employment the parallel computing technique, for example, to reduce the computing time of image analysis.

5. Summary

This study proposed an image analysis method to estimate crack opening development in a reinforced concrete (RC) tubular structure subjected to a cyclic displacement at its top. The image analysis results of one of the stereo imaging systems in the experiment (i.e., the north one) were presented in this paper. The crack opening fields were estimated by analyzing the displacement fields using the crack analysis method proposed in this paper.

Cracks as thin as 0.02–0.03 mm were difficult to detect to the naked

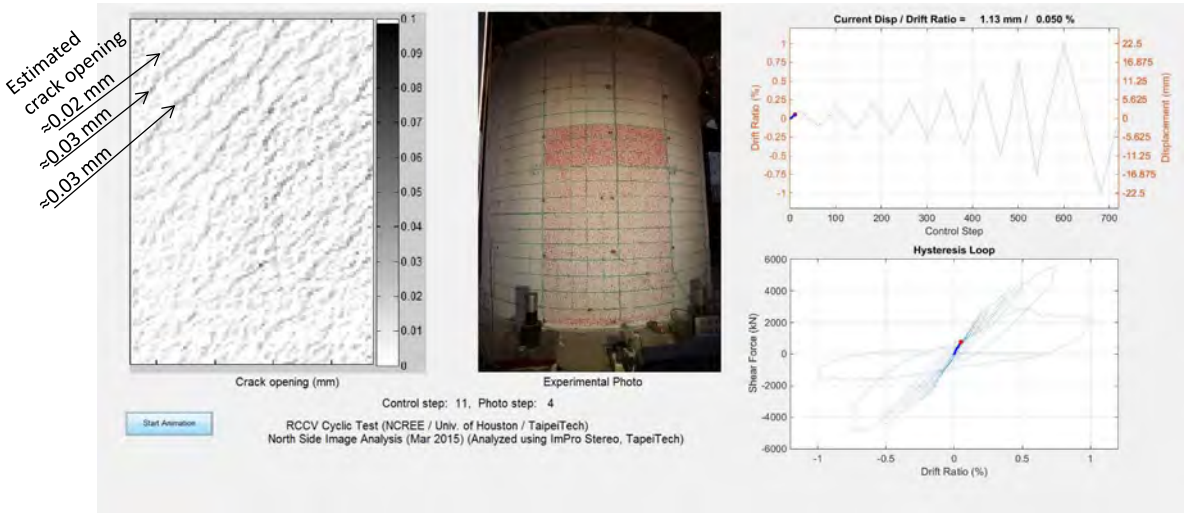

Fig. 17. Thin cracks observed by image analysis (drift ratio: 0.05%).

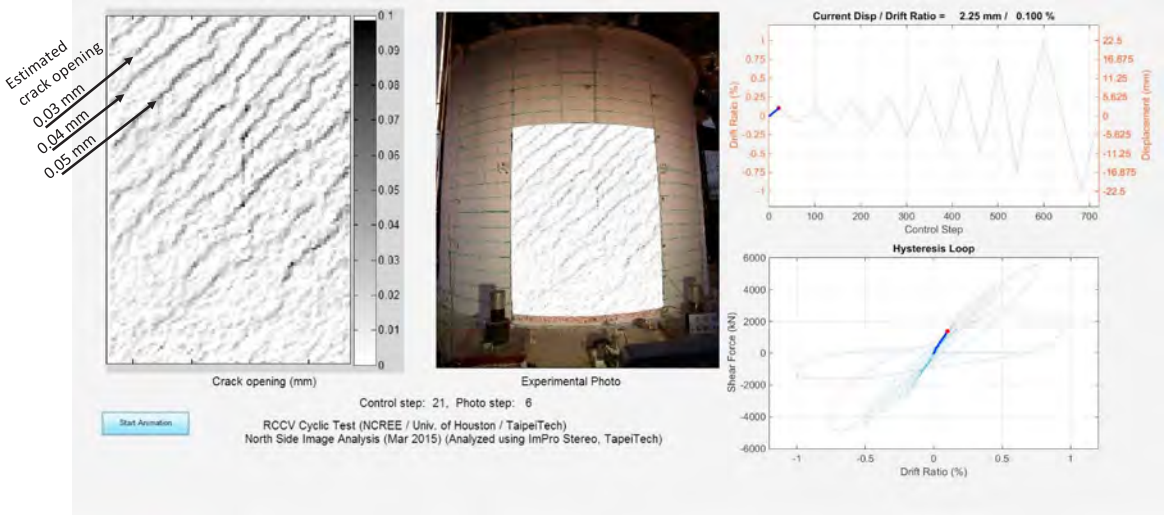

Fig. 18. Thin cracks observed by image analysis (drift ratio: 0.1%).

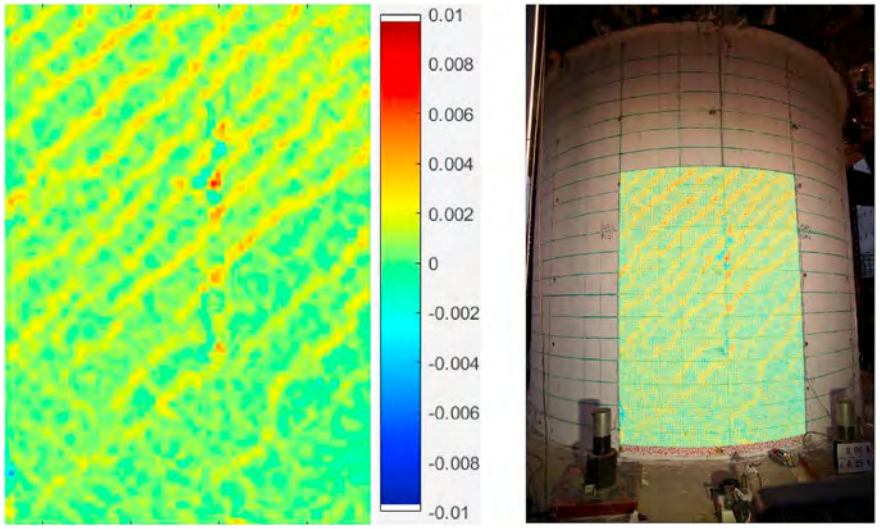

Fig. 19. Shear strain measurement by image analysis (drift ratio: 0.1%).

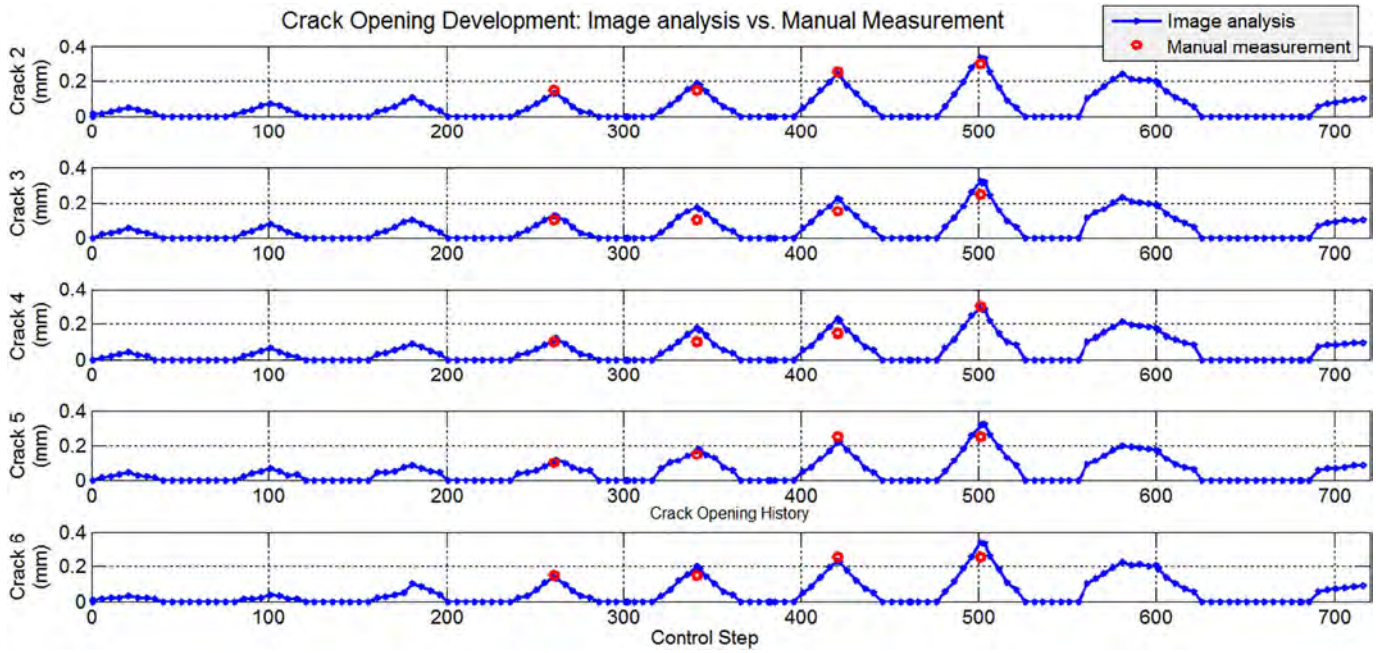

Fig. 20. Estimated crack opening history of selected cracks.

Table 3
Elapsed time statistics of image analysis using ImPro Stereo in this study.

Procedure	Manual operation time (second)[a]	Computing time for 163 step (second)	Computing time per step (second)
Camera calibration	300	10	0.06
Control point positioning	90	2621	16.08
Surface parameter calculation	20	1	0.01
Metric rectification	20	12,480	76.6
Optical flow analysis	20	231	1.42
Field analysis	20	10	0.06
Total	470	15,353	94.23

[a] Manual operation was estimated subjectively and can vary with different users.

eye, but could be clearly observed by image analysis. Crack opening width comparison between manual pen marks and image analysis showed that the differences were generally less than or equal to 0.03 mm. While manually marked cracks were available at only a few pause steps (seven steps in this study), image analysis provided dozens of steps of a continuous crack distribution and generated a video of crack changes. It also provided sufficient information to obtain crack opening width data of any part of any selected crack at a selected experimental time point.

This method is only applicable when cameras are firmly fixed and observed region is pre-painted with random patterns. To address these limitations, in follow-up studies, image analysis algorithms and methods can be further studied. Future algorithms can be developed to estimate camera movement by tracking predefined unmoving points or the background. Edge-detection- or machine-learning-based methods can be incorporated with the proposed method in cases where pre-painted patterns on the observed surfaces are insufficient.

Acknowledgments

The authors acknowledge the funding from the National Center for Research on Earthquake Engineering (NCREE) under project 06104A1600 and the Ministry of Science and Technology, Taiwan under projects MOST 104-2625-M-027-001 and MOST 105-2625-M-002-003. The RC containment vessel experiment could not have been successfully completed without technical assistance from Dr. K. J. Wang on experimental configuration and operations. We would like to thank Anthony Abram (www.uni-edit.net) for editing and proofreading this manuscript.

References

[1] T.T.C. Hsu, Y.L. Mo, Unified Theory of Concrete Structures, John Wiley & Sons, 2010, http://dx.doi.org/10.1002/9780470688892.
[2] E.L. Labib, Y.L. Mo, T.T.C. Hsu, Shear cracking of prestressed girders with high strength concrete, Concrete Struct. Mater. 7 (2013) 71–78, http://dx.doi.org/10.1007/s40069-013-0033-4.
[3] C. Arya, F.K. Ofori-Darko, Influence of crack frequency on reinforcement corrosion in concrete, Cem. Concr. Res. 26 (3) (1996) 345–353, http://dx.doi.org/10.1016/S0008-8846(96)85022-8.
[4] A. Akhavan, S.M.H. Shafaatian, F. Rajabipour, Quantifying the effects of crack width, tortuosity, and roughness on water permeability of cracked mortars, Cem. Concr. Res. 42 (2) (2012) 313–320, http://dx.doi.org/10.1016/j.cemconres.2011.10.002.
[5] ACI Committee 224, Causes, evaluation, and repair of cracks in concrete structures, ACI 224.1R-07, American Concrete Institute, USA, 2007, https://www.concrete.org/store/productdetail.aspx?ItemID=224107 , Accessed date: 1 January 2017.
[6] European Committee for Standardization, Eurocode 2: Design of Concrete Structures Part 1-1: General Rules and Rules for Buildings, EN1992-1-1, European Committee for Standardization, 2004, http://eurocodes.jrc.ec.europa.eu/doc/WS2008/EN1992_1_Walraven.pdf , Accessed date: 1 January 2017.
[7] J.D. Stevenson, Code for concrete reactor vessels and containments, Companion Guide to the ASME Boiler & Pressure Vessel Code, Second edition, vol. 1, ASME Press, USA, 2006, http://dx.doi.org/10.1115/1.802183.ch14.
[8] R.J. Janowiak, H.G. Ashar, C.A. Zalesiak, Evaluation of existing nuclear safety-related concrete structures, ACI 349.3R-02, American Concrete Institute, USA, 2002, https://www.concrete.org/store/productdetail.aspx?ItemID=349302 , Accessed date: 1 January 2017.
[9] C.H. Luu, Y.L. Mo, T.T.C. Hsu, Development of CSMM-based shell element for reinforced concrete structures, Eng. Struct. 132 (2017) 778–790, http://dx.doi.org/10.1016/j.engstruct.2016.11.064.
[10] A. Jefferson, R. Tenchev, A. Chitez, I. Mihai, G. Coles, P. Lyons, J. Ou, Finite element crack width computations with a thermo-hygro-mechanical-hydration model for concrete structures, Eur. J. Environ. Civ. En. 18 (7) (2014) 793–813, http://dx.doi.org/10.1080/19648189.2014.896755.
[11] F.J. Ma, A.K.H. Kwan, Crack width analysis of reinforced concrete members under flexure by finite element method and crack queuing algorithm, Eng. Struct. 105 (2015) 209–219, http://dx.doi.org/10.1016/j.engstruct.2015.10.012.
[12] C.H. Loh, K.J. Loh, Y.S. Yang, W.Y. Hsiung, Y.T. Huang, Vibration-based system identification of wind turbine system, Struct. Control Hlth. 24 (2017) e1877, http://dx.doi.org/10.1002/stc.1876.
[13] M. Omidvar, Z. Chen, M. Iskander, Image-based Lagrangian analysis of granular

kinematics, J. Comput. Civ. Eng. 29 (6) (2015) 04014101, http://dx.doi.org/10.1061/(ASCE)CP.1943-5487.0000433.
[14] S. Ali, Z. Toony, D. Laurendeau, A 3D vision-based inspection method for pairwise comparison of locally deformable 3D models, Mach. Vis. Appl. 26 (2015) 1061–1078, http://dx.doi.org/10.1007/s00138-015-0711-0.
[15] C. Sung, P.Y. Kim, 3D terrain reconstruction of construction sites using a stereo camera, Autom. Constr. 64 (2016) 65–77, http://dx.doi.org/10.1016/j.autcon.2015.12.022.
[16] M. Rodríguez-Martín, P. Rodríguez-González, S. Lagüela, D. González-Aguilera, Macro-photogrammetry as a tool for the accurate measurement of three-dimensional misalignment in welding, Autom. Constr. 71 (2016) 189–197, http://dx.doi.org/10.1016/j.autcon.2016.08.016.
[17] Y.J. Cha, K. You, W. Choi, Vision-based detection of loosened bolts using the Hough transform and support vector machines, Autom. Constr. 71 (2016) 181–188, http://dx.doi.org/10.1016/j.autcon.2016.06.008.
[18] J.G. Chen, N. Wadhwa, Y.J. Cha, F. Durand, W.T. Freeman, O. Büyüköztürk, Modal identification of simple structures with high-speed video using motion magnification, J. Sound Vib. 345 (2015) 58–71, http://dx.doi.org/10.1016/j.jsv.2015.01.024.
[19] T. Yu, A. Zhu, Y. Chen, Efficient crack detection method for tunnel lining surface cracks based on infrared images, J. Comput. Civ. Eng. 31 (3) (2017) 04016067, http://dx.doi.org/10.1061/(ASCE)CP.1943-5487.0000645.
[20] T.C. Hutchinson, Z. Chen, Improved image analysis for evaluating concrete damage, J. Comput. Civ. Eng. 20 (3) (2006) 210–216, http://dx.doi.org/10.1061/(ASCE)0887-3801(2006)20:3(210).
[21] H. Zakeri, F.M. Nejad, A. Fahimifar, Rahbin: a quadcopter unmanned aerial vehicle based on a systematic image processing approach toward an automated asphalt pavement inspection, Autom. Constr. 72 (2016) 211–235, http://dx.doi.org/10.1016/j.autcon.2016.09.002.
[22] J.H. Chen, M.C. Su, R. Cao, S.C. Hsu, J.C. Lu, A self organizing map optimization based image recognition and processing model for bridge crack inspection, Autom. Constr. 73 (2017) 58–66, http://dx.doi.org/10.1016/j.autcon.2016.08.033.
[23] G. Li, X. Zhao, K. Du, F. Ru, Y. Zhang, Recognition and evaluation of bridge cracks with modified active contour model and greedy search-based support vector machine, Autom. Constr. 78 (2017) 51–61, http://dx.doi.org/10.1016/j.autcon.2017.01.019.
[24] T.H. Dinh, Q.P. Ha, H.M. La, Computer vision-based method for concrete crack detection, Proceedings of the 14th International Conference on Control, Automation, Robotics & Vision. Phuket Thailand, 2016, http://dx.doi.org/10.1109/ICARCV.2016.7838682.
[25] P. Prasanna, K.J. Dana, N. Gucunski, B.B. Basily, H.M. La, R.S. Lim, H. Parvardeh, Automated crack detection on concrete bridges, IEEE Trans. Autom. Sci. Eng. 13 (2) (2014) 591–599, http://dx.doi.org/10.1109/TASE.2014.2354314.
[26] Y.J. Cha, W. Choi, O. Büyüköztürk, Deep learning-based crack damage detection using convolutional 6neural networks, Comput. Aided Civil Infrastruct. Eng. 32 (2017) 361–378, http://dx.doi.org/10.1111/mice.12263.
[27] Y.S. Yang, C.L. Wu, T.T. Hsu, Thin shear crack observation of a cylinder structure test using image analysis, Proceedings of the IEEE International Instrumentation and Measurement Technology Conference (I2MTC), Taipei, Taiwan, 2016, http://dx.doi.org/10.1109/I2MTC.2016.7520387.
[28] Y.S. Yang, S.H. Hsieh, K.C. Tsai, S.J. Wang, K.J. Wang, W.C. Cheng, C.W. Hsu, ISEE: Internet-based simulation for earthquake engineering—part I: database approach, Earthq. Eng. Struct. Dyn. 36 (2007) 2291–2306, http://dx.doi.org/10.1002/eqe.730.
[29] Y.S. Yang, C.M. Yang, C.W. Huang, Thin crack observation in a reinforced concrete bridge pier test using image processing and analysis, Adv. Eng. Softw. 83 (2015) 99–108, http://dx.doi.org/10.1016/j.advengsoft.2015.02.005.
[30] Y.S. Yang, C.W. Huang, C.L. Wu, A simple image-based strain measurement method for measuring the strain fields in an RC-wall experiment, Earthq. Eng. Struct. Dyn. 41 (2012) 1–17, http://dx.doi.org/10.1002/eqe.1111.
[31] ImPro Stereo, ImPro StereoImPro Stereo, the official website of ImPro Stereo, https://sites.google.com/site/improstereoen/home, (2015) , Accessed date: 1 January 2015.
[32] J.Y. Bouguet, Camera calibration toolbox for Matlab, A web page at http://www.vision.caltech.edu/bouguetj/, (2014) (Accessed 1 March 2014).
[33] G. Bradski, A. Kaehler, Learning OpenCV 3: Computer Vision in C++ With the OpenCV Library, O'Reilly Media, Inc., 2016, http://shop.oreilly.com/product/0636920044765.do , Accessed date: 1 January 2017.
[34] OpenCV, Open source computer vision, the official web site of OpenCV, http://www.opencv.org, (2017) (Accessed 1 Nov 2017).
[35] M. Hu, S. Ali, M. Shah, Learning motion patterns in crowded scenes using motion flow field, Proceedings of the 19th International Conference on Pattern Recognition (ICPR'08), Tampa, FL, USA, 2008, http://dx.doi.org/10.1109/ICPR.2008.4761183.
[36] M.R. Halfawy, J. Hengmeechai, Optical flow techniques for estimation of camera motion parameters in sewer closed circuit television inspection videos, Autom. Constr. 38 (2014) 39–45, http://dx.doi.org/10.1016/j.autcon.2013.10.016.
[37] Y.J. Cha, J.G. Chen, O. Büyüköztürk, Output-only computer vision based damage detection using phase-based optical flow and unscented Kalman filters, Eng. Struct. 132 (2017) 300–313, http://dx.doi.org/10.1016/j.engstruct.2016.11.038.
[38] M. Pedersoli, R. Timofte, T. Tuytelaars, L. Van Gool, An elastic deformation field model for object detection and tracking, Int. J. Comput. Vis. 111 (2) (2015) 137–152, http://dx.doi.org/10.1007/s11263-014-0736-2.
[39] Z. Zhu, K. Davari, Comparison of local visual feature detectors and descriptors for the registration of 3D building scenes, J. Comput. Civ. Eng. 29 (5) (2015) 04014071, http://dx.doi.org/10.1061/(ASCE)CP.1943-5487.0000381.
[40] C. Nonis, C. Niezrecki, T.Y. Yu, S. Ahmed, C.F. Su, T. Schmidt, Structural health monitoring of bridges using digital image correlation, Proceedings of the SPIE Smart Structures and Materials + Nondestructive Evaluation and Health Monitoring, 2013, San Diego, California, USA, 2013, http://dx.doi.org/10.1117/12.2009647.